Inside the electronic structure of the $Sm_3Fe_5O_{12}$ garnet: A mixed *ab initio* and experimental study

M. U. González-Rivas,[1,*] M. A. Ortiz-Medrano,[1] G. Herrera-Pérez,[2] G. G. Carbajal-Arízaga,[3] R. Flores-Moreno,[3] L. Fuentes-Cobas,[4] M. E. Fuentes-Montero,[5,†] and M. García-Guaderrama[1,‡]

[1]*Laboratorio de Materiales y Sistemas Fotosensibles, Departamento de Ingeniería de Proyectos, Centro Universitario de Ciencias Exactas e Ingenierías, Universidad de Guadalajara, Blvd. José Guadalupe Zuno 48, Industrial los Belenes, C.P. 45157, Zapopan, Jalisco, México*

[2]*Catedrático CONACyT assigned to Centro de Investigación en Materiales Avanzados, S. C., Miguel de Cervantes 120, C.P. 31136, Chihuahua, Chihuahua, México*

[3]*Departamento de Química, Universidad de Guadalajara, Marcelino García Barragán 1421, C.P. 44430 Guadalajara, Jalisco, México*

[4]*Centro de Investigación en Materiales Avanzados, S.C., Ave. Miguel de Cervantes 120, Complejo Industrial, C.P. 31136, Chihuahua, Chihuahua, México*

[5]*Facultad de Ciencias Químicas, Universidad Autónoma de Chihuahua, Circuito Universitario s/n campus II, C.P. 31125, Chihuahua, Chihuahua, México*

(Received 5 October 2020; revised 5 February 2021; accepted 6 July 2021; published 26 July 2021)

A combination of density functional theory (DFT) with experimental methods was used to study the electronic and crystal structure of $Sm_3Fe_5O_{12}$ (SmIG), which was synthesized using a modified sol-gel method. Computational studies were performed within the generalized gradient approximation (GGA), with and without the Hubbard-U correction (DFT+U), to analyze the influence of the on-site repulsion on the band structure and the density of states (DOS) of SmIG, as well as the structural parameters. The calculations were contrasted with experimental results from x-ray diffraction (XRD) and UV-Vis spectra. A Rietveld refinement returned a lattice parameter of 12.5231(3) Å. Synthesis methods seem to have a substantial effect in the band gap of SmIG, as our experimental value of 2.26–2.27 eV differs from the 2.02 eV value previously reported for samples prepared using the traditional solid-state method, despite similar lattice parameters. The DFT-calculated lattice parameters were within 1% of the experimental value. Analytically calculated effective Hubbard-U values were 4.3092 eV for tetrahedral iron, and 6.0926 eV for octahedral iron. A model is proposed to calculate the band gap in $Sm_3Fe_5O_{12}$, taking into account the structure's ferrimagnetism and energy level distribution. A direct transition between minority spin states was found, resulting in a calculated band gap of 2.27 eV, close to the aforementioned value from sol-gel synthesis.

DOI: 10.1103/PhysRevB.104.035151

I. INTRODUCTION

The garnet structure, corresponding to compounds with the formula $A_3B_2C_3O_{12}$, is described in the $Ia\bar{3}d$ space group (No. 230) [1]. Garnets have long fascinated scientists from fields as diverse as mineralogy, crystallography, physics, chemistry, and materials science. This is particularly true for the ferrimagnetic rare-earth iron garnets (REIGs), given their many different and interesting properties, which are as diverse as the compositions. They portray remarkable chemical and structural stability compared to other metal-oxide systems [2]. They have the highest Faraday rotation among currently known materials [3,4]. Furthermore, they also present other interesting phenomena such as magnetocrystalline anisotropy [5], thermochromism [6–8], a compensation temperature [9,10], among other characteristics.

This versatility has led to a variety of applications, with rare-earth garnets being particularly prominent in the emerging field of spintronics, where $Y_3Fe_5O_{12}$ (YIG) and its fellow REIGs fulfill a variety of roles [11–15]. In such applications their insulating behavior, coupled with the energy-level splitting associated with ferrimagnetism, makes them ideal media for spin-wave propagation.

In some ways, yttrium-iron garnet seems to be the logical choice over its rare-earth brethren, but it still has some limitations. In the realm of spintronics, YIG's main disadvantage is that its magnetic anisotropy is shape dominant, limiting some of its applications. This has led to renewed interest in garnet compositions where perpendicular magnetocrystalline anisotropy prevails [16]. Selected REIGs are among the few

*Present address: Department of Physics and Astronomy, University of British Columbia, Vancouver, British Columbia V6T 1Z1, Canada; mug3095@student.ubc.ca; mulises.gonzalez@alumnos.udg.mx

†Corresponding author: mfuentes@uach.mx

‡Corresponding author: marco.garcia@academico.udg.mx

such materials that are also ferrimagnetic. They are typically preferred over ferromagnetic materials, since the anisotropy is surface induced rather than intrinsic in the latter, imposing thickness constraints [17]. $Sm_3Fe_5O_{12}$ (samarium-iron garnet) is one such material. This property makes SmIG technologically relevant for proposed electric field control of magnetization in heavy metal/ferrimagnetic insulator interfaces, utilizing spin-orbit torque, in a niche in which its main competitor is $Tm_3Fe_5O_{12}$ [16]. Therefore, more studies surrounding SmIG are required to characterize the extent of its potential in such devices fully.

As previously mentioned, garnets are usually described within the $Ia\bar{3}d$ space group. The metal ions occupy crystallographic sites with no degrees of freedom, while oxygen takes the general 96*h* positions, enabling them to move in all three directions. In samarium-iron garnet (SmIG), the sites are 24*c* for Sm, 16*a* for octahedral iron, and 24*d* for tetrahedral iron [18]. The latter's spin is antiferromagnetically coupled to octahedral iron, with the 3:2 tetrahedral:octahedral stoichiometry resulting in ferrimagnetic behavior [1,19].

Notably, Sm has long been considered the largest ion that can fill the dodecahedral site in iron garnets and still yield a single-phase bulk product obtained by traditional methods. While reports on the synthesis of monophasic $Nd_3Fe_5O_{12}$ exist, they are limited to low temperature, single-crystal techniques such as hydrothermal growth [20], and liquid phase epitaxy (LPE) [21].

Kohn-Sham density functional theory (DFT) [22,23] provides an efficient theoretical framework for solving the electronic structure of materials within the independent electron approximation. Furthermore, current implementations yield highly reproducible results [24].

For all of DFT's strengths and versatility, problems arise when trying to describe strongly correlated systems, such as those containing rare-earth ions [25] or presenting magnetic behavior (or in this case, both of them). This is a consequence of the preponderance of density functionals being based on the electron gas, leading to overly delocalized states.

The most straightforward way of tackling the delocalization issue is implementing the Hubbard-U correction (DFT+U), where a repulsive energy term is added to the desired states, thus ensuring they adopt a localized distribution. In practice, DFT+U has proven to be a reliable way to improve agreement with experiment [19,25,26]. Moreover, it manages to describe a wide variety of phenomena while retaining conceptual simplicity [27,28].

However, studies on the electronic structure of iron garnets are scarce, despite their scientific and technological relevance. The few reports that exist center mainly on YIG [2,19,29,30], or the thin-film only bismuth-iron garnet (BIG) [31,32]. For REIGs, there are a pair of studies on $Gd_3Fe_5O_{12}$ [10,33], and a single article comprehending the entire lanthanide series [34]. The latter, however, focuses on structural predictions and magnetic behavior, providing detailed density of states (DOS) calculations only for $Gd_3Fe_5O_{12}$ and $Nd_3Fe_5O_{12}$. Thus, it is critical to study other members of the rare-earth iron-garnet family from a computational standpoint, as electronic structure plays a fundamental role in the properties of magnetic materials.

Electronic structure calculations on $Sm_3Fe_5O_{12}$ are particularly scarce. The work by Nakamoto *et al.* investigates the unit cell's parameter and magnetic moments of the ions [34], but there remains a lack of detailed band structure and density of states calculations. These results are particularly useful for spintronic devices, where the behavior of interest lies around E_F. The motivation of this work is to present a study of this material, using DFT algorithms, with and without the Hubbard-U correction. Their interpretation allows a deeper understanding of the origin of its electronic and magnetic properties. These calculations are complemented with experimental data, confirming the samarium-iron garnet phase's presence. Its lattice parameters were determined through the Rietveld refinement of x-ray diffraction patterns, and the sample's band gap through UV-Vis spectroscopy.

II. EXPERIMENTAL PROCEDURE

A. Sample preparation

Polycrystalline, phase pure powder samples of $Sm_3Fe_5O_{12}$ were obtained via a polyvinyl-alcohol (PVA) sol-gel technique, derived from the one reported for the synthesis of $BiFeO_3$ [35] and $YBa_2Cu_3O_{7-x}$ [36]. However, we did not find any reports on the preparation of iron garnets by such a route.

For the synthesis procedure, reagent-grade Sm_2O_3 (Aldrich, 99.9%) and $Fe(NO_3)_3 \cdot 9H_2O$ (Sigma-Aldrich, 98%) were used as Sm and Fe sources. A stoichiometric amount of HNO_3 (Sigma-Aldrich, 68%) was used to dissolve Sm_2O_3, giving $Sm(NO_3)_3$. Afterwards, $Fe(NO_3)_3 \cdot 9H_2O$ was incorporated into the resulting solution. Once iron nitrate was fully dissolved, a 10% wt PVA (Sigma-Aldrich, MW 89 000–98 000, 99.99%) solution was added in a 1:1 $OH^- : M^{3+}$ ratio.

The solution was then kept at 80 °C and stirred, at 120 rpm, until its volume suffered a drastic reduction, at which point it was transferred to a hot plate preheated to 250 °C. At this stage, a thick and airy foam, accompanied by a large production of gases, was observed. The product was thoroughly dried and maintained at 250 °C, until no nitric acid fumes were left. The resulting powders were then thoroughly grounded and calcined at 850–1150 °C to obtain $Sm_3Fe_5O_{12}$.

B. Sample characterization

Powder x-ray diffraction (XRD) measurements were carried out on a PANalytical Empyrean diffractometer with a Cu $K\alpha$ nonmonochromated radiation, operating at 200 mA, with a 50 kV accelerating voltage. The data were collected at room temperature in the $10^\circ \leqslant 2\theta \leqslant 80^\circ$ range, with a 0.01326° step size and 60 s time per step. ICSD-Desktop software [37] was employed for phase identification. Rietveld refinement [38] was performed using the July 2017 version of the Fullprof Suite for Mac [39,40], assuming a pseudo-Voigt peak shape. For specific details of the refinement procedure, the reader is referred to the Supplemental Material [41].

Scanning electron microscopy (SEM) images were obtained using a TESCAN MIRA 3 LMU field-emission microscope, operating at 10 kV. Samples were not sputter

coated to preserve the highly porous morphology. Lastly, the UV-Visible diffuse-reflectance spectra (UV-Vis-DRS) were collected at room temperature on a Cary 300 spectrophotometer, in a range of 200–800 nm, with a 0.3 nm step size and 0.1 s time per step.

C. Computational details

Solid-state DFT calculations were performed using the Vienna *ab initio* simulation package (VASP5.3) [42], using the projector augmented wave (PAW) method [43,44], under the generalized gradient approximation (GGA) with a Perdew-Burke-Entzerhof (PBE) exchange-correlation functional [45,46]. Calculations were also done under the GGA+U approximation. The primitive unit cell, which is half the size of the conventional unit cell, was used. This corresponds to 4 formula units.

PAW potentials were selected from the VASP database. The "Fe_pv_new" potential, which includes p electrons within the valence, for a total of 14 valence electrons, was used to describe the Fe atoms. For oxygen, the standard "O" potential with 6 valence electrons was selected. Finally, for Sm, the "Sm_3" potential was used, which treats the $4f$ electrons as frozen in the core, resulting in 11 valence electrons. This has been proven to be a reasonable approximation for triply ionized Sm [47]. Furthermore, UV-Vis spectra do not show any absorption peaks that can be attributed to charge transfer involving the Sm^{3+} ions. The features are instead associated with Fe^{3+}–O^{2-} interactions [7,8,48–51]. Therefore, Sm states are not expected to populate the lowest conduction states, which are what will concern the analysis in the present article. This approximation does have the disadvantage that Sm^{3+}'s magnetic moment is ignored, so care must be taken when drawing conclusions about the system's magnetic properties.

Alternatively, one can consider the description employed in this article the limit where Sm ions are ordered paramagnetically, while Fe ions remain antiferromagnetically coupled [34]. The electronic properties should not be affected, as it has been shown that to properly approximate E_g in REIGs with a less-than-half-filled $4f$ shell, one must apply the DFT+U correction to the RE ion. This term effectively localizes the electrons, if less extremely than taking them as part of the core. The end result is that the $4f$ conduction band shifts up in energy, while the valence band shifts down [34]. Perhaps more importantly, even complex electronic properties of REIGs have been reproduced regardless of the inclusion of $4f$ electrons as core states [33].

The plane-wave energy cutoff was set at 520 eV to obtain well-converged calculations. The electronic convergence criterion was 10^{-7} eV. A $4 \times 4 \times 4$ Monkhorst-Pack grid [52] for the k points in the first Brillouin zone, yielded results converged within 1 meV/atom and 0.6 kbar.

The structure was relaxed using a residual minimization-direct inversion in the iterative subspace (RMM-DIIS) algorithm [53], with a time step of 0.5 fs. The convergence criterion for the Hellmann-Feynman forces was set at 10^{-5} Å/eV. Density of states calculations used the tetrahedron method on a $12 \times 12 \times 12$ Γ-centered grid. Band structure calculations followed the standard procedure [19,30,54].

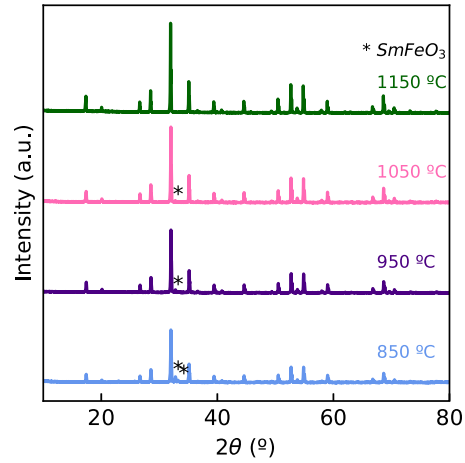

FIG. 1. Temperature evolution of the phase composition of samples synthesized using the sol-gel PVA route. All peaks, unless otherwise stated, belong to the garnet phase. At 1150 °C, single-phase $Sm_3Fe_5O_{12}$ is obtained.

The value of the Hubbard U parameter was obtained from a linear-response calculation, following the method of Cococcioni *et al.* [55], which has previously been applied to antiferromagnetically coupled iron ferrite systems such as $BiFeO_3$ [56]. Tetrahedral iron (Fe_T) and octahedral iron (Fe_O) were considered separately, each with their specific Hubbard-U value. The VASP code already treats the two sites as different species with their own wave function (otherwise ferrimagnetic order cannot be achieved). Therefore, it is straightforward to assign each site its own Hubbard parameter. Perhaps more importantly, within the framework of Cococcioni *et al.*, U is a function of both the electrons under consideration and the coordination of the ions, making octahedral and tetrahedral environments inequivalent. The structure was then relaxed again to account for the new energy term, leading to another set of calculations performed under the resulting geometry.

Other methods and levels of theory were also explored. Under the PBE+U framework, the effect of oxygen vacancies was investigated. Calculations were also performed under the local spin density approximation (LSDA) and the LSDA+U method, as implemented in the Quantum-ESPRESSO package [57,58]. The reader is referred to the Supplemental Material for these results [41].

The majority of calculations were post-processed using the PyProcar [59] and Pymatgen [60] python packages.

III. RESULTS AND DISCUSSION

A. Crystal structure analysis

Figure 1 shows the evolution of the powder XRD patterns with increasing temperature. They are indexed according to the ICSD database. At 850 °C the garnet structure (identified according to entry 23857) [61] is already the main phase present in the samples, although there is still a noticeable presence of peaks associated with $SmFeO_3$ (entry 27276) [62] as an impurity phase. By 1050 °C, said reflections are almost invisible, and at 1150 °C they are beyond the detection limits of the instrument, making this calcination temperature the

TABLE I. Phase percentages of $Sm_3Fe_5O_{12}$ and $SmFeO_3$ calculated using Rietveld refinement. Significant figures are reported.

T (°C)	$Sm_3Fe_5O_{12}$ (%)	$SmFeO_3$ (%)
850	87	13
950	95	5
1050	97	3
1150	100	N/A

chosen one. Rietveld refinement phase percentage analysis, summarized in Table I, confirms this conclusion.

Scanning electron microscopy (Fig. 2) reveals a highly porous, "foam" microstructure, with a high degree of agglomeration, which holds under higher magnification. This morphology is probably related to the drying process within the synthesis and the evaporation of PVA while calcinating. PVA is also probably responsible for the agglomeration, as it is frequently used as a binding agent in the sintering of ceramic powders.

Figure 3 presents the Rietveld refinement of the structure in the $Ia\bar{3}d$ space group. All peaks are associated with the garnet structure. A lattice parameter of 12.5231(3) Å was determined, in good agreement with the literature [63,64], with a nearly flat background indicating a high degree of crystallinity. The results of this analysis and quality of fit are shown in Table II. The sharp peaks and large crystallite seen from the micrographs render size analysis pointless. For a complete list of the refined parameters, the reader is referred to the Supplemental Material [41].

Table III presents a comparison between the relaxed lattice parameters, as predicted by different levels of theory within the DFT framework, and the experimental results from Rietveld refinement. While DFT constitutes a 0 K calculation with respect to the nuclei, the lattice parameter of $Sm_3Fe_5O_{12}$ varies about 0.01 Å from 20 to 300 K [63]. Therefore, the variation with respect to temperature is less than 0.1% of the measured value. Looking at the calculations' results it is immediately apparent that the PBE flavor of DFT without the Hubbard term provides a remarkable agreement with experimental results. Meanwhile, PBE+U calculations present a slight overestimation of the lattice parameters. This discrepancy is most certainly associated with the added repulsion introduced by the Hubbard term. Since electrons try to get away from each other, the unit cell tends to expand, with a larger unit cell reducing d-d electron interactions. Nevertheless, the lattice parameter remains within 1% of the observed experimental value. The calculated magnetic moments of the Fe ions in the structure and resulting magnetization of 3.7 μ_B/formula unit are in reasonable agreement with the previous report by Nakamoto *et al.* [34], as presented in Table IV.

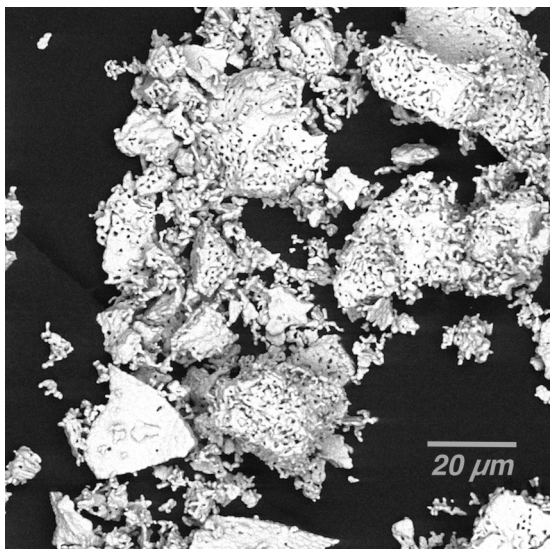

FIG. 2. SEM micrograph of $Sm_3Fe_5O_{12}$, showing a highly porous morphology. Sample synthesized using the sol-gel PVA procedure and calcined at 1150 °C for 4 h.

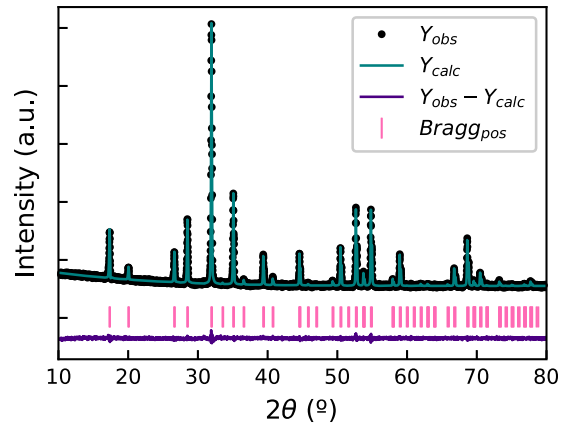

FIG. 3. Rietveld analysis of a $Sm_3Fe_5O_{12}$ powder diffraction pattern, collected at room temperature. The $Ia\bar{3}d$ space group was used for the structural model. This particular sample was calcined at 1150 °C for 4 h.

B. Electronic structure

A Kubelka-Munk transformation [65] (Fig. 4) was performed on the UV-Vis DRS spectra to obtain information regarding electronic excitations in the sample. Iron-garnet materials' optical properties are well understood to be associated with ligand-metal charge transfer and Fe^{3+} d-d transitions [8]. The latter are weaker because they correspond to forbidden transitions, which are allowed to happen, in this case, due to the breaking of degeneracy by the crystal field [66]. The corresponding regions are labeled in Fig. 4.

The charge transfer goes from occupied O_{2p} states to empty Fe_{3d} orbitals ($O^{2-} + Fe^{3+} \rightarrow O^{-} + Fe^{2+}$), located around 488 nm (2.54 eV) [7], while the d-d transitions occur between 1.35 and 2.04 eV [48–51]. The bands at 600 nm, along with the shoulder around 700 nm, are associated with octahedral iron ions, with the latter also having a contribution from tetrahedral iron. On a fundamental level, garnet powders are green because of the presence of these otherwise forbidden d-d transitions [8].

The band gap of SmIG was then estimated from the corresponding Tauc plot, following Kubelka-Munk theory [67–70] (Fig. 5). The transition is of the direct-allowed type, with an estimated value of 2.26–2.27 eV, in reasonable agreement

TABLE II. Results of the Rietveld analysis presented in Fig. 3.

Space group					$Ia\bar{3}d$ (230)
Lattice parameter a (Å)					12.5231(3)
Atom	Oxidation number	Wyckoff position	x	y	z
O	2−	96h	−0.0307(3)	0.0535(3)	0.1496(4)
Fe	3+	16a	0	0	0
Fe	3+	24d	0.375	0	0.25
Sm	3+	24c	0.125	0	0.25
Rietveld reliability factors: R_p, R_{wp}, χ^2					26.6, 10.3, 1.357

with the literature for $Sm_3Fe_5O_{12}$ powders synthesized by the sol-gel route [71].

The information gleaned from UV-Vis analysis can then be contrasted with electronic structure calculations. The PBE band structure of $Sm_3Fe_5O_{12}$ is shown in Fig. 6. This description illustrates some essential features of SmIG, such as the presence of a band gap, although it is severely underestimated, a well-known DFT problem. Another important feature is that the conduction minima and valence maxima are located at the same point in the IBZ for both spin channels. This arrangement implies a direct electronic transition, which occurs at the Γ point.

Unfortunately, inspecting the density of states (DOS) for this level of theory reveals a significant delocalization of valence iron states, as shown in Fig. 7. Given SmIG's insulating properties, the associated states are expected to be more localized in nature. This behavior is a clear indication that the description of this system can be improved. However, PBE does reproduce the spin dependence of the DOS, a hallmark of a magnetic material. It can also be seen that Fe_T orbitals are strongly hybridized with O states in the spin-up valence region. Meanwhile, for the spin-down valence, the hybridization is mostly between Fe_O and O sites.

PBE+U band-structure calculations (Fig. 8) were performed under the framework of Dudarev *et al.* [72]. An $U_{\text{eff}} = 4.3092$ eV for tetrahedral iron (Fe_T) and $U_{\text{eff}} = 6.0926$ eV for octahedral iron (Fe_O) were obtained from the linear-response approach of Cococcioni *et al.* [55]. The results from the PBE+U level of theory are much more reasonable and in better agreement with experiment, while preserving the desirable features that were already present in the PBE description of the system. The band gap is still a direct transition located at the Γ point within the IBZ, albeit with a much larger value. It is a better approximation to what was observed in the UV-Vis experiment. Also, the bands display the spin dependence expected for a magnetic material. Meanwhile, the Fermi level is located at the top of the valence band, the expected behavior for an insulator.

Figure 9 presents the projected density of states (PDOS) of SmIG under the PBE+U description of samarium-iron garnet. These results can be considered in terms of the ones obtained by Nakamoto *et al.* [34]. Said work presents density of states plots only for $Gd_3Fe_5O_{12}$ and $Nd_3Fe_5O_{12}$, using $U = 4$ eV for both iron sites. Looking at said two compositions, it can be inferred with reasonable certainty that the energy level distribution for iron ions is largely unaffected by the rare earth occupying the c site. With that in mind, it is possible to look at the effect of employing different values of U, compared to an approach where ions of the same chemical nature species share the value of the Hubbard-U parameter. The goal here is to analyze whether using the analytical result of separate parameters results in significant differences in the electronic structure of the REIGs. This effect is expected to be particularly relevant when considering E_g, as its value is directly related to the value of the U parameter [73]. As the choice of rare earth does not exert a significant influence on the energy level distribution of iron ions, U_{eff} then becomes our primary tool in modeling their behavior within a self-consistent DFT framework. It is immediately evident that using separate values of U_{eff} for each site does change Fe's energy level distribution and the wave functions' localization, owing to the different levels of electronic repulsion.

Compared to Nakamoto *et al.*'s results, Fig. 9 displays a stronger spin and coordination dependence of the iron ions' distribution. These changes can clearly be attributed to the ≈2 eV difference in electronic interactions introduced to Fe_T and Fe_O ions. The different degrees of repulsion, predicted from a strictly theoretical method, will prove important when analyzing the energy level distribution around the valence band and its relationship with approximating E_g for optical transitions in a ferrimagnetic system.

TABLE III. Lattice parameters for $Sm_3Fe_5O_{12}$. The general oxygen positions are also reported, as they are the only atoms free to move within the structure.

Result	a (Å)	Error (%)	O_x	O_y	O_z
PBE	12.5231	0.0	−0.0290	0.0548	0.1494
PBE+U	12.6435	0.96	−0.0279	0.0545	0.1499
Expt.	12.5231(3)	–	−0.0307(3)	0.0535(3)	0.1496(4)

TABLE IV. Calculated magnetic moment for iron ions in $Sm_3Fe_5O_{12}$.

	U (eV)		μ (μ_B)		
Result	Fe_T	Fe_O	Fe_T	Fe_O	Ref.
LSDA+U	4.9	2.4	3.5	−3.6	This work
PBE+U	4.3	6.1	4.1	−4.3	This work
PBE+U	4	4	4.1	−4.2	[34]

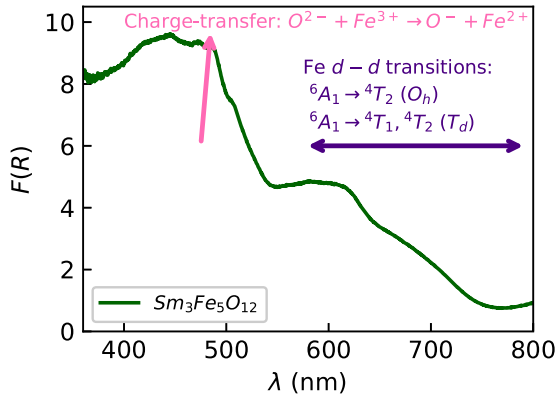

FIG. 4. Kubelka-Munk transformed reflectance (absorbance) vs wavelength for $Sm_3Fe_5O_{12}$ synthesized by the sol-gel PVA route. The sample was calcined at 1150 °C for 4 h.

The energy level distribution presented here allows for a deeper understanding of the charge-transfer mentioned in the analysis of Fig. 4. Said transfer, located at 2.54 eV, is associated with the onset of conduction.

Understanding the distribution presented in the PDOS is paramount to calculate $Sm_3Fe_5O_{12}$'s band gap from computational results and compare it to experiment. Looking at Fig. 9 it is clear that states with strong oxygen character dominate near the top of the valence band. Conversely, tetrahedral iron states account for the lowest part of the conduction band. Furthermore, the transition must happen between bands with the same spin direction. This result follows from the garnet structure's antiferromagnetic coupling [74] and the Pauli exclusion principle applied to Fe^{3+}, as illustrated in Figs. 10(b) and 10(c). It is then reasonable to expect the transition to take place between spin-down valence O and conduction Fe_T states, a proposition which shall now be analyzed in detail. For most materials, identifying the difference between the absolute maximum of the valence band and the absolute minimum of the conduction band with E_g would be a valid hypothesis. It shall however be explained why this proposal is inappropriate for $Sm_3Fe_5O_{12}$. It is important to remember that the states in a ferrimagnetic material present a spin dependence. As a consequence, there are two conduction band minima and two valence band maxima, which need not be equal. In the $Sm_3Fe_5O_{12}$ case, going from the maximum of the valence band to the bottom of the conduction band corresponds to a spin-flip transition, known as the Stoner gap [75]. While this situation could be easily overlooked, when comparing computational results to experiment it is important to remember the selection rules for UV-Vis spectroscopy. They state that dipole-allowed (optical) electronic transitions must be spin conserving. Mathematically, $\Delta S = 0$, so no spin-flip transition is expected to occur. Of course this still leaves two possibilities, one per spin channel. However, it is immediately evident that the energy gap E_g will be different between the spin-down and spin-up directions. And yet, experimental band-gap measurements typically return a single value. It can be surmised that the corresponding E_g value will be the one with the smallest magnitude, but it is pertinent to check whether this assumption makes physical sense in SmIG.

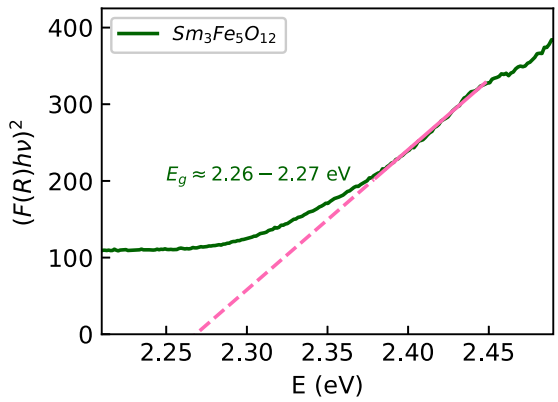

FIG. 5. Tauc plot for the UV-Vis DRS spectra of $Sm_3Fe_5O_{12}$. The dashed line indicates the extrapolation used for the band-gap value estimation.

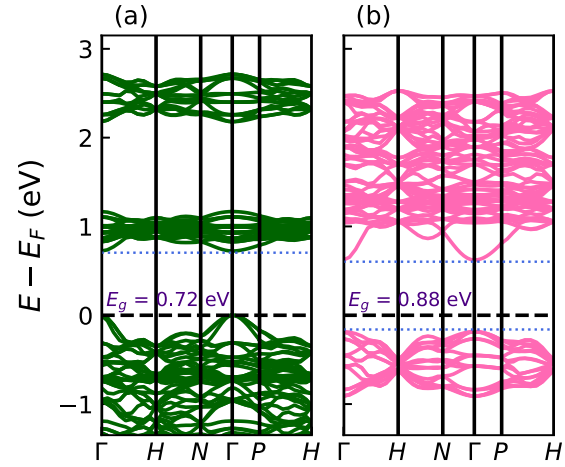

FIG. 6. Band structure of $Sm_3Fe_5O_{12}$ calculated under the PBE functional. (a) Majority spin channel (spin up). (b) Minority spin channel (spin down).

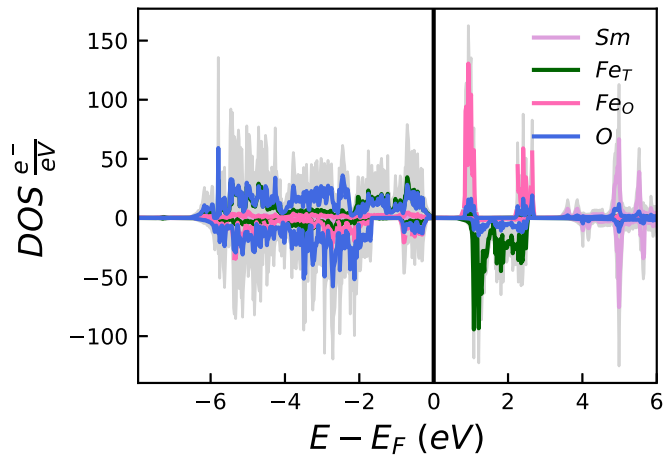

FIG. 7. Projected density of states (PDOS) for $Sm_3Fe_5O_{12}$, calculated under the PBE flavor of the GGA approximation. The sign of the DOS indicates the spin direction. Valence iron states are highly delocalized, indicating that the description of the system can be improved upon. The shaded area corresponds to the total DOS.

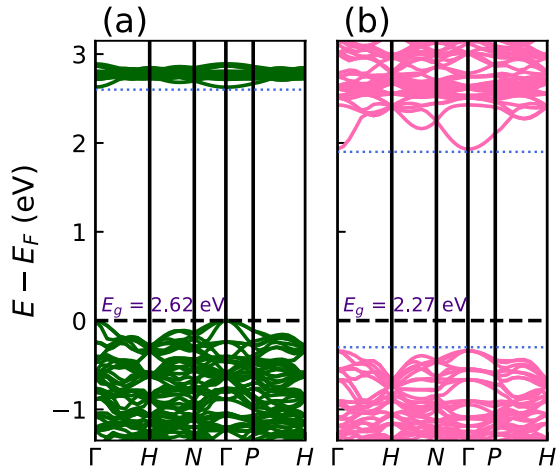

FIG. 8. PBE+U band structure of $Sm_3Fe_5O_{12}$. The energy gap in each spin direction is indicated. (a) Majority spin (up). (b) Minority spin (down). A clear improvement in the description of the band gap is observed.

With the calculations and experimental evidence at hand, it is possible to construct a model for the magnetic coupling of ions in the garnet structure. As previously mentioned, the UV-Vis transitions observed in Fig. 4 point to the formation of Fe^{2+} and O^- at the onset of charge transfer. It is then reasonable to expect the electronic configuration of the first excited state to involve an Fe^{2+} and an O^- ion.

As Fe^{3+} has a $3d^5$ electron configuration, for Fe^{2+} to form, additional electrons must come from a band with an opposite spin to the previously occupied orbitals. Otherwise, a spin-flip excitation would have to take place, which has already been ruled out. Valence Fe_T corresponds to majority spin (spin up), so its conduction states must belong to the minority spin channel (spin down). As can be seen in Figs. 10(a) and 10(b), the top of the minority channel's valence band is made of oxygen states. These arguments agree with the previous analysis of the PDOS. The most logical option for the first excited state

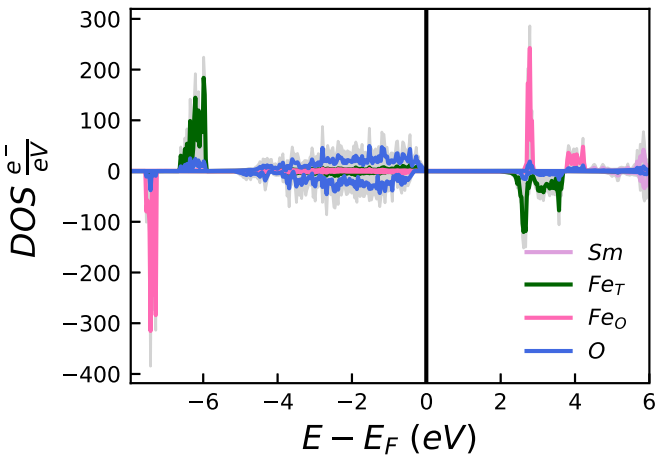

FIG. 9. Projected density of states (PDOS) for samarium-iron garnet within the DFT+U model. A clear improvement is observed in the description of valence iron states, which are now highly localized, as expected. The shaded area represents the total DOS.

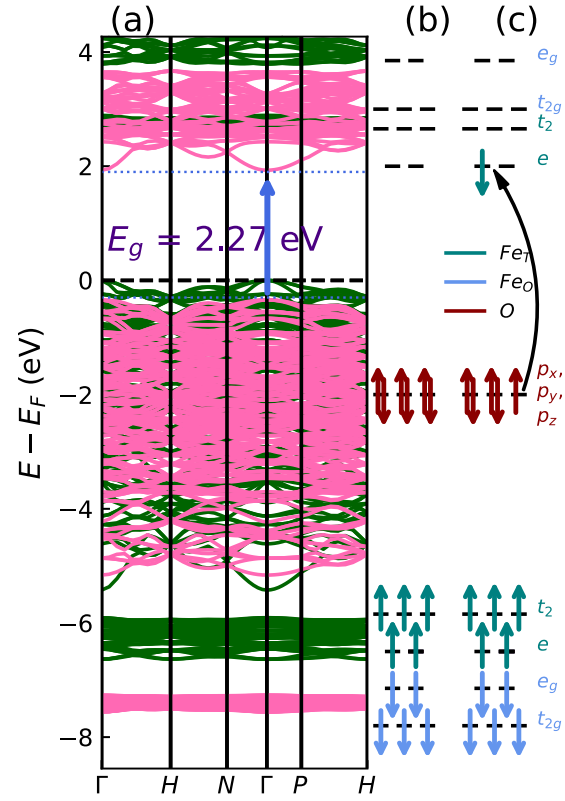

FIG. 10. Proposed model for the magnetic coupling and energy level distribution ions within the samarium-iron garnet structure. (a) Band structure with the correct band gap for SmIG. Dark green lines denote spin-up bands, while light pink ones correspond to the spin-down channel. The E_g transition happens between spin-down bands at the Γ point. The calculated band-gap value of 2.27 eV is very close to the one we found for sol-gel PVA synthesized SmIG. (b) Energy level distribution for the ground state, as determined from DFT calculations and crystal field theory. (c) Energy level distribution for the first excited state, illustrating charge transfer from oxygen to tetrahedral iron.

is then that an O^{2-} ion should transfer an electron to an Fe_T^{3+} ion, taking said electron from the top of the spin-down valence band to the bottom of the spin-down conduction band. One can therefore identify the band gap shown in Fig. 10(c) as corresponding to the experimental measurement presented in Fig. 5, consistently with the previous consideration that the minority channel's band gap is smaller than the majority channel's. Fortunately, the calculated value of 2.27 eV is remarkably close to the experimentally measured 2.26–2.27 eV.

Such a good agreement between experimental and computational results indicates that PBE+U does an excellent job describing the electronic structure of samarium-iron garnet, and that the model is correct in its interpretation of electronic transitions in iron garnets. To further validate the results, a quick review of the literature is presented in Table V. This reveals that although SmIG's band-gap measurements are scarce, the value for a sol-gel synthesized material is practically equal to our sample's [71], and therefore also close to DFT+U's prediction.

Meanwhile, materials synthesized by the conventional solid-state route were previously reported to have a smaller

TABLE V. Calculated band gap and lattice parameter of $Sm_3Fe_5O_{12}$ from experimental and theoretical results.

Method	a (Å)	E_g (eV)	Ref.
PBE	12.5231	0.80	This work
PBE+U	12.6435	2.27	This work
LSDA	12.1654	None	Suppl. Mater. [41]
LSDA+U	12.3388	1.13	Suppl. Mater. [41]
Sol-gel PVA	12.5231(3)	2.26–2.27	This work
Solid state	12.5350(4)	2.02	[71]
Sol-gel	12.5413(4)	2.28	[71]

value of around 2.02 eV. This may seem confusing at first glance, but one must consider that the traditional ceramic route suffers from poor crystallinity, broad particle-size distribution, nonstoichiometry, and inhomogeneous composition compared to sol-gel and other wet-chemical syntheses [76,77], and that grain boundaries can also play a significant role in the observed electronic properties of materials [78]. These factors make the behavior of solid-state-synthesized materials difficult to model, while sol-gel materials should remain closer to an ideal single crystal. The fact that our value agrees with the previous results for sol-gel methods despite a noticeable difference in lattice parameter (0.018 Å) and synthesis procedure supports this notion.

Table V also presents the results from the additional calculations mentioned in Sec. II C, illustrating why the PBE and PBE+U approximations were chosen. LSDA and LSDA+U give a much worse prediction of $Sm_3Fe_5O_{12}$'s band gap, differing by more than 10% of the experimental value. Their predictions of the material's lattice parameter are also much worse. Meanwhile, for the vacancies model, the band gap was severely overestimated, a clear indication that something is off with this description. This body of evidence is enough to determine PBE and PBE+U (without vacancies) as the best methods under consideration in this work.

IV. CONCLUSIONS

In this work, DFT+U calculations on the electronic structure of the $Sm_3Fe_5O_{12}$ garnet have been reported. A new synthesis method, via a modified sol-gel route, has been implemented as well. Using PBE and PBE+U GGA, the resulting band structure and densities of states, both as stand alone results and in terms of their relationship with the experimentally measured electronic structure, were detailed. The effective Hubbard U parameters were calculated analytically according to the method of Cococcioni *et al.* and determined to be $U_{\text{eff}} = 4.3092$ eV for tetrahedral iron (Fe_T) and $U_{\text{eff}} = 6.0926$ eV for octahedral iron (Fe_O). Using U_{eff} for each ion proved to be important in reproducing the electronic structure of iron garnets. Considering the $4f$ electrons of Sm^{3+} as *core* electrons does not seem to impact the calculations negatively. While additional levels of theory were also considered, PBE and PBE+U were determined to be the best at capturing the system's physics.

A model is proposed to elucidate how the band gap should be calculated for samarium-iron garnet, taking into account its ferrimagnetic behavior and energy level distribution. Since the densities of states of rare-earth iron garnets do not depend on the choice of rare-earth ion within the regime where the latter is paramagnetically ordered (corresponding to keeping the rare-earth's electrons "frozen" in the core), the presented model is expected to hold for other REIGs, as long as different U_{eff} are considered for each iron site. The predicted E_g of 2.27 eV under this model agrees very well with the experimentally observed 2.26–2.27 eV for sol-gel PVA synthesized SmIG, along with the previously reported 2.28 eV for $Sm_3Fe_5O_{12}$ (synthesized by the citrate sol-gel method). At the same time, there is a more significant difference with reports for materials obtained using the traditional ceramic route, where E_g is reported to be 2.02 eV.

Combined with predicted lattice parameters and atomic positions very close to the ones obtained from Rietveld refinement, these results indicate that a PBE+U description of $Sm_3Fe_5O_{12}$ is more than sufficient to study its basic electronic structure. This conclusion is further supported by the agreement of the calculated magnetic moment of the iron ions with previous results for $Sm_3Fe_5O_{12}$.

The discrepancy observed for solid-state band-gap values seems to indicate that crystallinity and/or grain boundary effects play a significant role in the electronic properties of iron garnets.

ACKNOWLEDGMENTS

The authors thank L. A. Montero and M. E. Montero-Cabrera for insightful discussion and suggestions during the drafting process. Most of the computational studies required for this work were carried out at the Centro de Análisis de Datos y Supercómputo (CADS) at Universidad de Guadalajara. Computational resources available at the department of Chemistry of Universidad Autónoma de Chihuahua and Centro de Investigación en Materiales Avanzados, S.C. are also thankfully acknowledged. The authors are also grateful for the technical support of F. Orozco at CADS, J. P. Palomares-Baez at Universidad Autónoma de Chihuahua, R. Domínguez-García at Centro de Investigación en Materiales Avanzados, S.C., and Sergio Oliva at Universidad de Guadalajara. M. A. Ortiz-Medrano and M. U. González-Rivas each thank CONACyT for financial support in the form of a scholarship for national master's studies, Grants No. 1009320 and No. 961326, respectively. G. Herrera-Pérez acknowledges Cátedra Grant No. 2563 of CONACyT.

[1] S. Geller and M. A. Gilleo, The crystal structure and ferrimagnetism of yttrium-iron garnet, $Y_3Fe_2(FeO_4)_3$, J. Phys. Chem. Solids **3**, 30 (1957).

[2] P. Baettig and T. Oguchi, Why are garnets not ferroelectric? A theoretical investigation of $Y_3Fe_5On_{12}$, Chem. Mater. **20**, 7545 (2008).

[3] A. D. Block, P. Dulal, B. J. Stadler, and N. C. Seaton, Growth parameters of fully crystallized YIG, Bi:YIG, and Ce:YIG films with high Faraday rotations, IEEE Photonics J. **6**, 1 (2014).

[4] M. Guillot, H. Le Gall, J. M. Desvignes, and M. Artinian, Low-temperature anisotropy of the Faraday rotation in the samarium iron garnet, J. Appl. Phys. **70**, 6401 (1991).

[5] F. Hansteen, A. Kimel, A. Kirilyuk, and T. Rasing, Femtosecond Photomagnetic Switching of Spins in Ferrimagnetic Garnet Films, Phys. Rev. Lett. **95**, 047402 (2005).

[6] H. Liu, L. Yuan, H. Qi, S. Wang, Y. Du, Y. Zhang, C. Hou, and S. Feng, In-situ optical and structural insight of reversible thermochromic materials of $Sm_{3-x}Bi_xFe_5O_{12}$ ($x = 0$, 0.1, 0.3, 0.5), Dyes Pigments **145**, 418 (2017).

[7] H. Liu, L. Yuan, S. Wang, H. Fang, Y. Zhang, C. Hou, and S. Feng, Structure, optical spectroscopy properties and thermochromism of $Sm_3Fe_5O_{12}$ garnets, J. Mater. Chem. C **4**, 10529 (2016).

[8] H. Serier-Brault, L. Thibault, M. Legrain, P. Deniard, X. Rocquefelte, P. Leone, J. L. Perillon, S. Le Bris, J. Waku, and S. Jobic, Thermochromism in yttrium iron garnet compounds, Inorg. Chem. **53**, 12378 (2014).

[9] T. Bayaraa, C. Xu, D. Campbell, and L. Bellaiche, Tuning magnetization compensation and Curie temperatures in epitaxial rare earth iron garnet films, Phys. Rev. B **100**, 214412 (2019).

[10] D. Campbell, C. Xu, T. Bayaraa, and L. Bellaiche, Finite-temperature properties of rare-earth iron garnets in a magnetic field, Phys. Rev. B **102**, 144406 (2020).

[11] M. Collet, O. Gladii, M. Evelt, V. Bessonov, L. Soumah, P. Bortolotti, S. O. Demokritov, Y. Henry, V. Cros, M. Bailleul, V. E. Demidov, and A. Anane, Spin-wave propagation in ultrathin YIG based waveguides, Appl. Phys. Lett. **110**, 092408 (2017).

[12] B. Divinskiy, N. Thiery, L. Vila, O. Klein, N. Beaulieu, J. Ben Youssef, S. O. Demokritov, and V. E. Demidov, Submicrometer near-field focusing of spin waves in ultrathin YIG films, Appl. Phys. Lett. **116**, 062401 (2020).

[13] R. Peña-Garcia, Y. Guerra, F. R. de Souza, L. A. Gonçalves, and E. Padrón-Hernández, The extended Bloch's law in yttrium iron garnet doped with Zn, Ni and Co, Physica E **103**, 354 (2018).

[14] M. Collet, X. De Milly, O. D'Allivy Kelly, V. V. Naletov, R. Bernard, P. Bortolotti, J. Ben Youssef, V. E. Demidov, S. O. Demokritov, J. L. Prieto, M. Muñoz, V. Cros, A. Anane, G. De Loubens, and O. Klein, Generation of coherent spin-wave modes in yttrium iron garnet microdiscs by spin-orbit torque, Nat. Commun. **7**, 10377 (2016).

[15] Q. Wang, B. Heinz, R. Verba, M. Kewenig, P. Pirro, M. Schneider, T. Meyer, B. Lägel, C. Dubs, T. Brächer, and A. V. Chumak, Spin Pinning and Spin-Wave Dispersion in Nanoscopic Ferromagnetic Waveguides, Phys. Rev. Lett. **122**, 247202 (2019).

[16] E. R. Rosenberg, L. Beran, C. O. Avci, C. Zeledon, B. Song, C. Gonzalez-Fuentes, J. Mendil, P. Gambardella, M. Veis, C. Garcia, G. S. D. Beach, and C. A. Ross, Magnetism and spin transport in rare-earth-rich epitaxial terbium and europium iron garnet films, Phys. Rev. Mater. **2**, 094405 (2018).

[17] P. Li, T. Liu, H. Chang, A. Kalitsov, W. Zhang, G. Csaba, W. Li, D. Richardson, A. DeMann, G. Rimal, H. Dey, J. S. Jiang, W. Porod, S. B. Field, J. Tang, M. C. Marconi, A. Hoffmann, O. Mryasov, and M. Wu, Spin-orbit torque-assisted switching in magnetic insulator thin films with perpendicular magnetic anisotropy, Nat. Commun. **7**, 12688 (2016).

[18] G. F. Dionne, *Magnetic Oxides* (Springer, New York, 2009), pp. 1–466.

[19] L. S. Xie, G. X. Jin, L. He, G. E. W. Bauer, J. Barker, and K. Xia, First-principles study of exchange interactions of yttrium iron garnet, Phys. Rev. B **95**, 014423 (2017).

[20] L. Guo, K. Huang, Y. Chen, G. Li, L. Yuan, W. Peng, H. Yuan, and S. Feng, Mild hydrothermal synthesis and ferrimagnetism of $Pr_3Fe_5O_{12}$ and $Nd_3Fe_5O_{12}$ garnets, J. Solid State Chem. **184**, 1048 (2011).

[21] V. J. Fratello, C. D. Brandle, S. E. Slusky, A. J. Valentino, M. P. Norelli, and R. Wolfe, Growth of single-crystal $Nd_3Fe_5O_{12}$ and $Pr_3Fe_5O_{12}$ Garnets, J. Cryst. Growth **75**, 281 (1986).

[22] P. Hohenberg and W. Kohn, Inhomogeneous electron gas, Phys. Rev. **136**, B864 (1964).

[23] W. Kohn and L. J. Sham, Self-consistent equations including exchange and correlation effects, Phys. Rev. **140**, A1133 (1965).

[24] K. Lejaeghere, G. Bihlmayer, T. Björkman, P. Blaha, S. Blügel, V. Blum, D. Caliste, I. E. Castelli, S. J. Clark, A. Dal Corso, S. De Gironcoli, T. Deutsch, J. K. Dewhurst, I. Di Marco, C. Draxl, M. Dułak, O. Eriksson, J. A. Flores-Livas, K. F. Garrity, L. Genovese *et al.*, Reproducibility in density functional theory calculations of solids, Science **351**, aad3000 (2016).

[25] A. Majid, W. Akram, and A. Dar, DFT study of electronic and structural properties of Sm:GaN, Comput. Mater. Sci. **88**, 71 (2014).

[26] A. Ismail, J. Hooper, J. B. Giorgi, and T. K. Woo, A DFT+U study of defect association and oxygen migration in samarium-doped ceria, Phys. Chem. Chem. Phys. **13**, 6116 (2011).

[27] J. Hubbard and B. H. Flowers, Electron correlations in narrow energy bands, Proc. R. Soc. London Ser. A **276**, 238 (1963).

[28] The Hubbard model at half a century, Nat. Phys. **9**, 523 (2013).

[29] Z. Rák, R. C. Ewing, and U. Becker, Electronic structure and thermodynamic stability of uranium-doped yttrium iron garnet, J. Phys.: Condens. Matter **25**, 495502 (2013).

[30] S. Tao, H. Chao, D. Hailong, Y. Wenlong, L. Hongchen, and W. Xinlao, First principles study of structure, electronic and optical properties of $Y_3Fe_5O_{12}$ in cubic and trigonal phases, Mater. Sci. Poland **33**, 169 (2015).

[31] O. Tohru, S. Shugo, and N. Kenji, First-principles study of spin-orbit interactions in bismuth iron garnet, J. Phys. Soc. Jpn. **74**, 401 (2005).

[32] F. Iori, A. Teurtrie, L. Bocher, E. Popova, N. Keller, O. Stéphan, and A. Gloter, Bismuth iron garnet: *Ab initio* study of electronic properties, Phys. Rev. B **100**, 245150 (2019).

[33] T. Bayaraa, C. Xu, Y. Yang, H. Xiang, and L. Bellaiche, Magnetic-Domain-Wall-Induced Electrical Polarization in Rare-Earth Iron Garnet Systems: A First-Principles Study, Phys. Rev. Lett. **125**, 067602 (2020).

[34] R. Nakamoto, B. Xu, C. Xu, H. Xu, and L. Bellaiche, Properties of rare-earth iron garnets from first principles, Phys. Rev. B **95**, 024434 (2017).

[35] T. Liu, Y. Xu, and J. Zhao, Low-temperature synthesis of $BiFeO_3$ via PVA sol-gel route, J. Am. Ceram. Soc. **93**, 3637 (2010).

[36] Y. K. Sun and I. H. Oh, Preparation of ultrafine $YBa_2Cu_3O_{7-x}$ superconductor powders by the poly(vinyl alcohol)-assisted sol-gel method, Ind. Eng. Chem. Res. **35**, 4296 (1996).

[37] D. Zagorac, H. Müller, S. Ruehl, J. Zagorac, and S. Rehme, Recent developments in the Inorganic Crystal Structure Database: Theoretical crystal structure data and related features, J. Appl. Crystallogr. **52**, 918 (2019).

[38] H. M. Rietveld, Line profiles of neutron powder-diffraction peaks for structure refinement, Acta Crystallogr. **22**, 151 (1967).

[39] J. Rodríguez-Carvajal, Recent advances in magnetic structure determination by neutron powder diffraction, Physica B **192**, 55 (1993).

[40] T. Roisnel and J. Rodríguez-Carvajal, WinPLOTR: A Windows Tool for Powder Diffraction Pattern Analysis, in *European Powder Diffraction EPDIC 7*, Materials Science Forum, Vol. 378 (Trans Tech Publications, 2001), pp. 118–123.

[41] See the Supplemental Material at http://link.aps.org/supplemental/10.1103/PhysRevB.104.035151 for details of the Rietveld refinement procedure, the parameters and results of LSDA and LSDA+U calculations done in Quantum-ESPRESSO, and the effect of introducing oxygen vacancies on the electronic structure of $Sm_3Fe_5O_{12}$.

[42] G. Kresse and J. Furthmüller, Efficient iterative schemes for *ab initio* total-energy calculations using a plane-wave basis set, Phys. Rev. B **54**, 11169 (1996).

[43] P. E. Blöchl, Projector augmented-wave method, Phys. Rev. B **50**, 17953 (1994).

[44] G. Kresse and D. Joubert, From ultrasoft pseudopotentials to the projector augmented-wave method, Phys. Rev. B **59**, 1758 (1999).

[45] J. P. Perdew, K. Burke, and M. Ernzerhof, Generalized Gradient Approximation Made Simple, Phys. Rev. Lett. **77**, 3865 (1996).

[46] R. Elmer, M. Berg, L. Carlen, B. Jakobsson, B. Noren, A. Oskarsson, G. Ericsson, J. Julien, T.F. Thorsteinsen, M. Guttormsen, G. Lovhoiden, V. Bellini, E. Grosse, C. Muntz, P. Senger, and L. Westerberg, Erratum of Generalized gradient approximation made simple, Phys. Rev. Lett. **78**, 1396(E) (1997).

[47] N. Bork, K. E. J. Eurenius, J. Rossmeisl, C. S. Knee, and T. Vegge, The atomic structure of protons and hydrides in $Sm_{1.92}Ca_{0.08}Sn_2O_{7-\delta}$ pyrochlore from DFT calculations and FTIR spectroscopy, J. Appl. Phys. **112**, 33705 (2012).

[48] S. H. Wemple, S. L. Blank, J. A. Seman, and W. A. Biolsi, Optical properties of epitaxial iron garnet thin films, Phys. Rev. B **9**, 2134 (1974).

[49] P. G. Manning, Optical absorption spectra of Fe^{3+} in octahedral and tetrahedral sites in natural garnets, Canadian Mineral. **11**, 826 (1972).

[50] K. A. Wickersheim and R. A. Lefever, Absorption spectra of ferric iron-containing oxides, J. Chem. Phys. **36**, 844 (1962).

[51] D. L. Wood and J. P. Remeika, Effect of impurities on the optical properties of yttrium iron garnet, J. Appl. Phys. **38**, 1038 (1967).

[52] J. D. Pack and H. J. Monkhorst, Special points for Brillouin-zone integrations, Phys. Rev. B **16**, 1748 (1977).

[53] P. Pulay, Convergence acceleration of iterative sequences. The case of SCF iteration, Chem. Phys. Lett. **73**, 393 (1980).

[54] Y.-N. Xu and W. Y. Ching, Electronic structure of yttrium aluminum garnet $Y_3Al_5O_{12}$, Phys. Rev. B **59**, 10530 (1999).

[55] M. Cococcioni and S. de Gironcoli, Linear response approach to the calculation of the effective interaction parameters in the LDA+*U* method, Phys. Rev. B **71**, 035105 (2005).

[56] I. A. Kornev, S. Lisenkov, R. Haumont, B. Dkhil, and L. Bellaiche, Finite-Temperature Properties of Multiferroic $BiFeO_3$, Phys. Rev. Lett. **99**, 227602 (2007).

[57] P. Giannozzi, S. Baroni, N. Bonini, M. Calandra, R. Car, C. Cavazzoni, D. Ceresoli, G. L. Chiarotti, M. Cococcioni, I. Dabo, A. D. Corso, S. de Gironcoli, S. Fabris, G. Fratesi, R. Gebauer, U. Gerstmann, C. Gougoussis, A. Kokalj, M. Lazzeri, L. Martin-Samos *et al.*, QUANTUM ESPRESSO: A modular and open-source software project for quantum simulations of materials, J. Phys.: Condens. Matter **21**, 395502 (2009).

[58] P. Giannozzi, O. Andreussi, T. Brumme, O. Bunau, M. Buongiorno Nardelli, M. Calandra, R. Car, C. Cavazzoni, D. Ceresoli, M. Cococcioni, N. Colonna, I. Carnimeo, A. Dal Corso, S. de Gironcoli, P. Delugas, R. A. DiStasio, A. Ferretti, A. Floris, G. Fratesi, G. Fugallo *et al.*, Advanced capabilities for materials modelling with Quantum ESPRESSO, J. Phys.: Condens. Matter **29**, 465901 (2017).

[59] U. Herath, P. Tavadze, X. He, E. Bousquet, S. Singh, F. Muñoz, and A. H. Romero, PyProcar: A Python library for electronic structure pre/post-processing, Comput. Phys. Commun. **251**, 107080 (2020).

[60] S. P. Ong, W. D. Richards, A. Jain, G. Hautier, M. Kocher, S. Cholia, D. Gunter, V. L. Chevrier, K. A. Persson, and G. Ceder, Python Materials Genomics (pymatgen): A robust, open-source python library for materials analysis, Comput. Mater. Sci. **68**, 314 (2013).

[61] F. Euler and J. A. Bruce, Oxygen coordinates of compounds with garnet structure, Acta Crystallogr. **19**, 971 (1965).

[62] M. Marezio, J. P. Remeika, and P. D. Dernier, The crystal chemistry of the rare earth orthoferrites, Acta Crystallogr. Sect. B **26**, 2008 (1970).

[63] M. Guillot, D. Rodic, and M. Mitric, Temperature dependencies of the lattice constants and thermal expansion coefficients of $Sm_3Fe_5O_{12}$ and $Er_3Fe_5O_{12}$ single crystals, J. Appl. Phys. **73**, 6304 (1993).

[64] M. Brahma, Aakansha, V. M. Gaikwad, and S. Ravi, Investigation of structural, magnetic and dielectric properties of Al-doped samarium iron garnet, Appl. Phys. A **125**, 333 (2019).

[65] P. Kubelka and F. Munk, Ein beitrag zur optik der farbanstriche, Z. Tech. Physik **12**, 259 (1931).

[66] V. K. Sankaranarayanan and N. S. Gajbhiye, Spectrochemical investigations of ultrafine amorphous and crystalline rare earth iron garnets, J. Solid State Chem. **93**, 134 (1991).

[67] R. López and R. Gómez, Band-gap energy estimation from diffuse reflectance measurements on sol-gel and commercial TiO_2: A comparative study, J. Sol-Gel Sci. Technol. **61**, 1 (2012).

[68] M. Nowak, B. Kauch, and P. Szperlich, Determination of energy band gap of nanocrystalline SbSI using diffuse reflectance spectroscopy, Rev. Sci. Instrum. **80**, 4 (2009).

[69] M. L. Myrick, M. N. Simcock, M. Baranowski, H. Brooke, S. L. Morgan, and J. N. McCutcheon, The Kubelka-Munk diffuse reflectance formula revisited, Appl. Spectrosc. Rev. **46**, 140 (2011).

[70] S. S. Abdullahi, S. Güner, Y. Koseoglu, I. Murtala, B. I. Adamu, and M. I. Abdulhamid, Simple method for the determination of band gap of a nanopowdered sample using Kubelka

Munk theory, J. Nigerian Assoc. Math. Phys. (NAMP) **35**, 241 (2016).

[71] H. Liu, L. Yuan, H. Qi, Y. Du, S. Wang, and C. Hou, Size-dependent optical and thermochromic properties of $Sm_3Fe_5O_{12}$, RSC Adv. **7**, 37765 (2017).

[72] S. L. Dudarev, G. A. Botton, S. Y. Savrasov, C. J. Humphreys, and A. P. Sutton, Electron-energy-loss spectra and the structural stability of nickel oxide: An LSDA+U study, Phys. Rev. B **57**, 1505 (1998).

[73] J. Zaanen, G. A. Sawatzky, and J. W. Allen, Band Gaps and Electronic Structure of Transition-Metal Compounds, Phys. Rev. Lett. **55**, 418 (1985).

[74] W. Noun, E. Popova, F. Bardelli, Y. Dumont, R. Bertacco, A. Tagliaferri, M. Tessier, M. Guyot, B. Berini, and N. Keller, Determination of yttrium iron garnet superexchange parameters as a function of oxygen and cation stoichiometry, Phys. Rev. B **81**, 054411 (2010).

[75] N. Janke-Gilman, K. N. Altmann, F. J. Himpsel, and R. F. Willis, Tuning the spin-flip gap in transition-metal magnets by alloying, Phys. Rev. B **72**, 064420 (2005).

[76] B. Robertz, F. Boschini, R. Cloots, and A. Rulmont, Importance of soft solution processing for advanced $BaZrO_3$ materials, Int. J. Inorganic Mater. **3**, 1185 (2001).

[77] W. Wen and J. M. Wu, Nanomaterials via solution combustion synthesis: A step nearer to controllability, RSC Adv. **4**, 58090 (2014).

[78] L. Liu, H. Fan, P. Fang, and X. Chen, Sol-gel derived $CaCu_3Ti_4O_{12}$ ceramics: Synthesis, characterization and electrical properties, Mater. Res. Bull. **43**, 1800 (2008).